Modeling and tracking control of a novel XYθz stage

Kunhai Cai[1], Yanling Tian[1,2], Fujun Wang[1], Dawei Zhang[1], Xianping Liu[2], Bijan Shirinzadeh[3]

[1]Key Laboratory of Mechanism Theory and Equipment Design of Ministry of Education, Tianjin University, Tianjin 300072, China

[2]School of Engineering, University of Warwick, Coventry CV4 7AL, UK

[3]Robotics and Mechatronics Research Laboratory, Department of Mechanical and Aerospace Engineering, Monash University, Clayton, VIC 3800, Australia

Abstract: A $XY\theta_z$ stage is designed and experimentally tested. This developed stage is driven by three piezoelectric actuators (PZTs) and guided by a flexure hinge based mechanism with three symmetric T-shape hinges. It was manufactured monolithically by using wire electrical discharge machining (WEDM) technology. In addition, considering the both electrical and mechanical characteristics, a third-order dynamic model of the 3-DOF system has been established to investigate the relationship between the input voltage and the output displacement of the entire system. The parameters of the third-order dynamic model were estimated by using the system identification toolbox. Furthermore, decoupling control is also proposed to solve the existed coupling motion of the stage. In order to compensate the hysteresis of PZT, the inverse Bouc-Wen model was utilized as a feedforward hysteresis compensator. Finally, extensive experiments were performed to verify the good decoupling and tracking performances of the developed stage.

Keywords: $XY\theta_z$ stage, Piezoelectric actuators, Dynamic model, Tracking control

1. Introduction

Nanopositioners are commonly used in various academic and industrial fields, such as micro/nano manipulation system, microelectronics processing, optical instruments and measurement systems. For example, in scanning probe microscopy systems, the nanopositioners are used to control an ultra-sharp tip relative to a sample surface for machining, imaging, and manipulating objects at nanometer scale [1, 2]. In addition, it is also one of the key components of thermosonic bonding equipments [3]. Precision positioning system is mainly composed of actuation device, guide mechanism and end effector. The piezoelectric actuator (PZT) is a good choice as actuation device, because it can provide excellent resolution actuation with high stiffness and high output force. In order to guarantee positioning accuracy, one of the best choices is to utilize flexure based mechanism as guidance of the motion, due to the advantages of flexure hinges including no backlash, free of wear, no lubrication, and low friction.

In the past few decades, parallel flexures have been confirmed to be applicable for the micro/nano positioning mechanism. For example, Stewart and Delta mechanisms [4, 5], are widely utilized on account to provide adequate motions in spatial or planar applications. The flexure based mechanisms are generally developed by replacing the conventional joints of the conventional parallel mechanism with flexure hinges. Therefore, design of the flexure hinges is a key issue. In the literature, there are a variety of flexure hinges that have been proposed and utilized in the precision positioning system, including notch-type hinge [6-8], leaf-spring hinge

[9-11], right elliptical hinge [12], V-shape flexure hinge [13], cross-axis flexural pivots [14-16], split-tube flexural pivots [17], cartwheel hinges [18-22], and so on. Among these proposed flexure hinges, the notch-type hinge and leaf-spring hinge are the most popular and widely utilized in precision positioning systems. Especially, the leaf-spring hinges are capable of achieving large working range. In this paper, the proposed T-shape flexure hinge consists of three leaf-spring hinges subsections connected together like a T-joint. Benefiting from this design, the movement of the special hinge is more flexible.

In the structural design of flexure-guided nanopositioners, many novel mechanisms are used in the micro/nano positioning domain. For example, Tian et al. developed a 5-bar mechanism for micro/nano operations [23, 24]. And design of a 2-DOF precision positioning platform featuring the parallelogram decoupling mechanisms [25]. Qin et al. [26, 27] focused on the designs of two different type decoupling positioning stages with 2-DOF. Wang et al. [28-30] designed a high-acceleration precision positioning system with a novel flexible decoupling mechanism. Polit and Dong [31] developed a high-bandwidth and decoupling XY positioning stage. In order to implement the positioning and orientation of the sample for the precision measurement and characterization, it is necessary to develop a $XY\theta_z$ positioning stage which can be utilized to conduct the in-plane motion. Tian et al. have designed a 3-DOF flexure-based mechanism for micro/nano manipulation [5]. Qin et al. proposed a design of a novel 3-DOF monolithic manipulator with three improved Scott-Russell (ISR) mechanisms [31]. Guo proposed a $XY\theta_z$ stage with the

parallelogram decoupling mechanisms [33]. In these developed mechanisms, a series of the notch-type hinges have been adopted as a guide mechanism. However, the mechanical design of the 3-DOF positioning system with combination of the notch type and leaf-spring hinges has also been provided by Kim et al. [34] and Bhagat et al. [35]. In addition, Kim et al. presented the mechanical design of a 3-DOF flexure-based parallel compliant mechanism for the hollow type biomedical specimen stage base on notch-type hinges and cartwheel hinges [36]. In this paper, the proposed $XY\theta_z$ stage is guided by a flexure hinge based mechanism with three symmetric T-shape hinges, and each T-shape flexure hinge mechanism consists of three leaf-spring hinge subsections connected together like a T-joint. The structure of the stage is more simple and compact by the symmetrical arrangement of the T-shape flexure hinge.

In current research efforts on piezo-driven compliant mechanisms, the control voltage is generally adopted as the input during the dynamics modeling. However, in the dynamic modeling, the PZT is generally modeled as a force generator with a built-inspring-damper component. It is common to define the driving force as the input into the system in the dynamics modeling. Other characteristics of the PZT are generally ignored. However, Tian [37] proposed the PZT could be electrically considered as a capacitance with an equivalent circuit. Similar modeling approach has been used in [47-49].

Since the control voltage is generally adopted as the input during operation, the hysteresis and creep nonlinearities of the PZT are included in the actual measurement.

It is easily observed that the existence of hysteresis loop in the measured results. Therefore, the piezo-driven compliant mechanism also suffers from the hysteresis of the PZT. In the past decade, different hysteresis models [38,40,41,43,45] have been established. It would be very desirable to remove the nonlinearities of the PZT in the dynamics modeling and identification.

In this paper, a novel $XY\theta_z$ stage is designed and experimentally tested. The remainder of this paper is organized as follows: Section II introduces the mechanical the design of the 3-DOF (Degree of Freedom) stage and prototype development. In Section III, a dynamic model of the system is established, and system identification is then implemented. The experimental tests are conducted in Section IV, and Section V concludes this paper.

2. Mechanical design and prototype development

The solid model of the 3-DOF stage is shown in Fig. 1. The parallel driven configuration is utilized in the design. It can be seen that the stage is mainly composed of three piezoelectric actuators (PZTs), three T-shape flexure hinge mechanisms, a moving platform and a base. Three T-shape flexure hinge mechanisms are located at the same circle with the separation angle of 120 °. Each T-shape flexure hinge mechanism consists of three leaf-spring hinge (I, II and III) subsections connected together like a T-joint as shown in Fig. 2. One end of each T-shape flexure hinge mechanism is connected to the moving platform and the others are fixed on the base. On the same circumference of the T-shape flexure hinge mechanism, there are three slots to install PZTs with the separation angle of 120 °. Each slot separates from

the T-shape flexure hinge mechanism with an angle of 60 °. The PZT can be preloaded through the behind fine screw bolt. By controlling the PZTs simultaneously, the moving platform can implement the translations in the X and Y directions, and rotation about the Z axis.

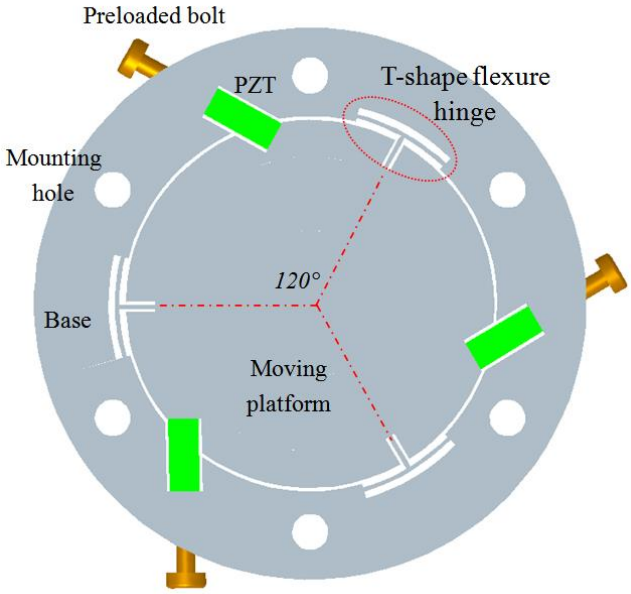

Figure 1 3D solid model of the developed 3-DOF stage

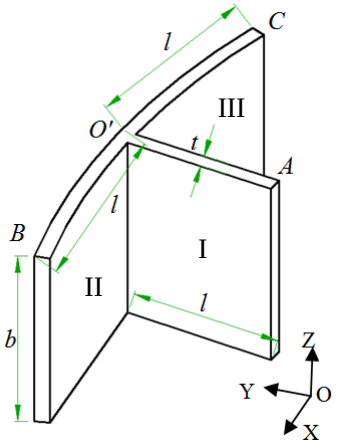

Figure 2 Schematic diagram of the T-shape flexible hinge structure

The proposed 3-DOF stage was manufactured monolithically using wire electrical discharge machining (WEDM) technology, and the material was selected as

Aluminum 7075-T6 with a Young's modulus of 72 GPa, a yield strength in excess of 434 MPa. The top and bottom surfaces were machined using a milling machine to guarantee the parallelism. Subsequently, artificial aging treatment method was utilized to release the residual stress. Considering that the T-shape flexible hinge mechanism must be inside the small and compact stage, the following parameters were determined: the stage diameter is chosen as ϕ 150 mm, the thickness is set as 18 mm, and the moving platform diameter is chosen as ϕ 100 mm. Therefore, three leaf-spring hinges have the same hinge width of b=18 mm. The geometric parameters of the T-shape flexible hinge are listed in Table I.

Table I: Geometric parameters of the T-shape flexible hinge.

Geometric parameters	t	l	b
Value(mm)	1.0	10.0	18.0

In order to examine the performance of the stage described above, modal analysis is performed to examine the dynamic characteristics of the stage using finite element analysis package ANSYS Workbench software. The material for the stage is chosen as Aluminum 7075-T6 with a density of 2770 kg/m3, a Young's modulus of 71 GPa, and a Poisson's ratio of 0.33. In order to improve the computational accuracy, the mapping mesh method is adopted. The mesh is strictly controlled in the areas of flexure hinges, where the large deformation is generally occurred. The results are shown in Fig. 3. When the piezoelectric actuators are not installed on the stage, the first mode shape is the rotation about the Z-axis, and its frequency is 528.11Hz; the second and third modes shape are the translations along the X and Y axes,

respectively, with the corresponding frequencies of 626.92 Hz and 626.95 Hz. If the PZTs are installed, it can be realized by incorporating spring-damper components into the stage. It is considered as a spring with a constant stiffness *k*, and one end of the spring is fixed and the other end is attached on the moving platform. The simulation results show that the first three natural frequencies increase to 806.04 Hz, 801.13 Hz and 931.20 Hz, and the corresponding mode shapes are the moving platform translating in the Y-axis and X-axis, and rotating about the Z axis, respectively.

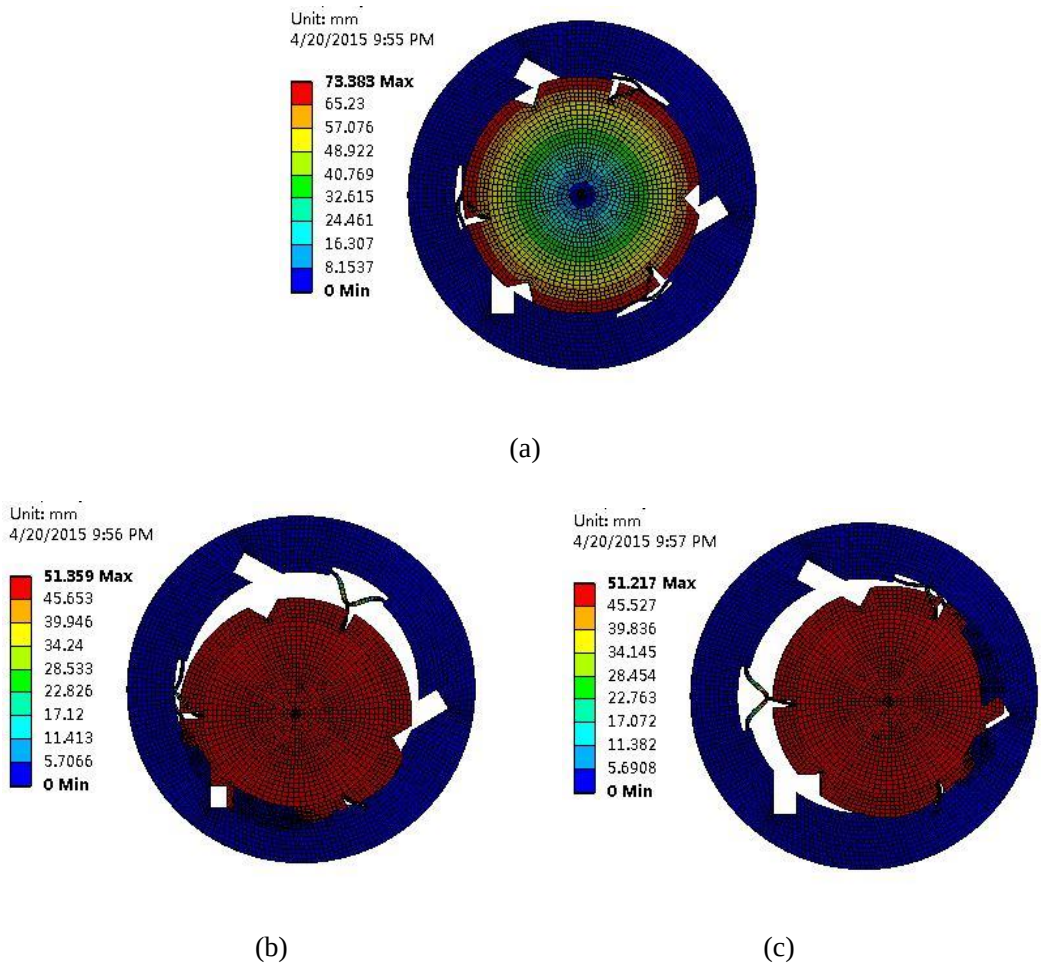

Figure 3 First three mode shapes of the 3-DOF stage with no PZTs installed: (a) first mode shape (528.11Hz), (b) second mode shape (626.92Hz) and third mode shape (626.95Hz).

According to the above characteristics analysis, it validates that the stage can provide both translational and rotational motions. In addition, the stage has a high natural frequency, which ensures that the system has good dynamic characteristics.

The prototype of the developed $XY\theta_z$ stage is shown in Fig. 4. The 3-DOF stage is mounted on a Newport RS-4000 optical table to reduce the ground vibrations. Three AE0505D18 PZTs were used with the maximum displacement of 15μm under the input voltage of 100V. The dSPACE DS1103 controller was used to generate the controlling signal, and the PI E-505.00 amplifier was used to amplify the signal to drive the PZTs. Three KEYENCE laser displacement sensors LK-H050 were used to measure the motion of the stage.

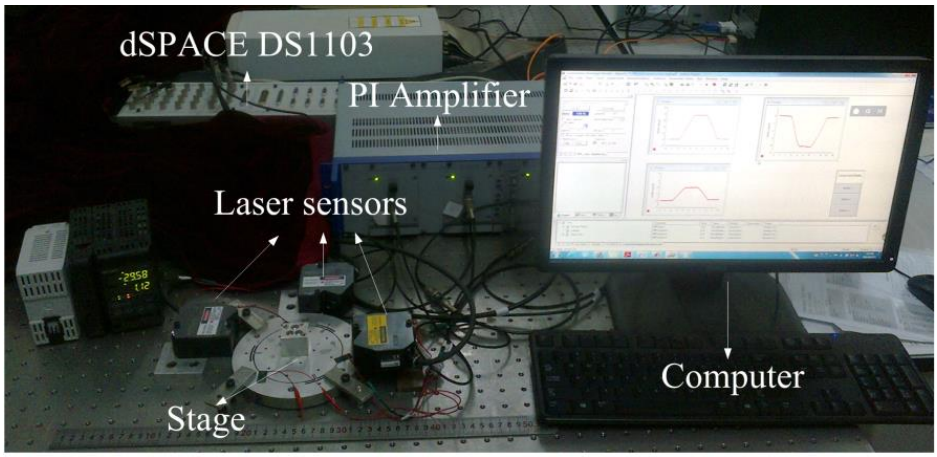

Figure 4 Experimental setup of the stage

3. Dynamics modeling and system identification

3.1 Dynamics modeling

The model of the stage can be considered as mass and spring system, and it is shown in Fig. 5. Based on the Newton's second law of motion, the differential equations for the dynamic motion of the flexure mechanism are given as Eq. (1). The dynamic model is established based on the assumption that only first three modes are

considered and all higher modes are neglected.

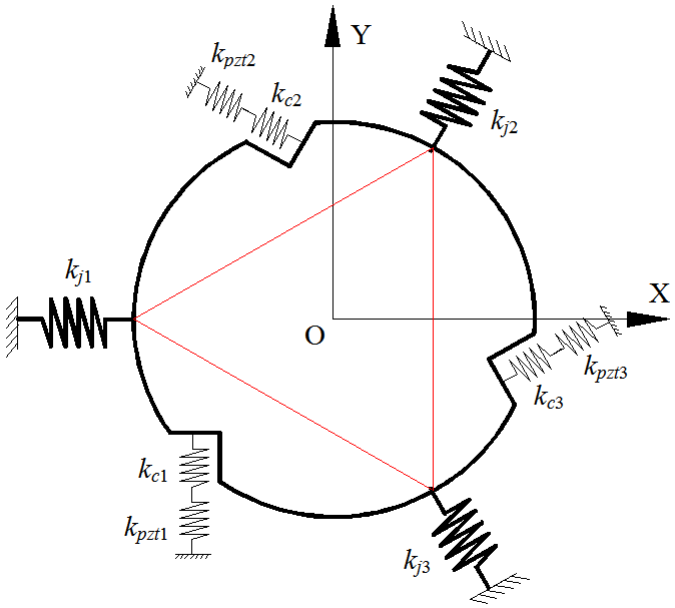

Figure 5 Dynamics model of the 3-DOF stage

$$\boldsymbol{M}\begin{bmatrix}\ddot{x}\\ \ddot{y}\\ \ddot{\theta}\end{bmatrix}+\boldsymbol{A}c_{eqx}\begin{bmatrix}\dot{x}\\ \dot{y}\\ \dot{\theta}\end{bmatrix}+\boldsymbol{A}k_{eqx}\begin{bmatrix}x\\ y\\ \theta\end{bmatrix}=\boldsymbol{BF} \tag{1}$$

where: $\mathbf{M}=Diag(m_{eq}\quad m_{eq}\quad I_{zz})$, $\mathbf{A}=Diag(3/2\quad 3/2\quad 3r^2)$

$$\boldsymbol{B}=\begin{bmatrix}0 & \sqrt{3}/2 & -\sqrt{3}/2\\ 1 & -1/2 & -1/2\\ r & r & r\end{bmatrix},\quad \boldsymbol{F}=\begin{bmatrix}f_{pzt1} & f_{pzt2} & f_{pzt3}\end{bmatrix}^T,\quad k_{eqx}=k_{jx}+\frac{k_{pzt}\cdot k_c}{k_{pzt}+k_c}$$

f_{pzt} represents the driving force of the PZT, m_{eq}, c_{eq} and I_{zz} denote the equivalent mass, the equivalent damping coefficient of the stage and moment of inertia about the Z-axis, respectively, k_{eqx} is the X-axis linear stiffness of the stage, k_{jx} is the X-axis equivalent stiffness of the "T" type flexible hinge, k_{pzt} is the stiffness of PZT, k_c is the equivalent Hertzian contact stiffness, r is the radius of the moving platform. **B** is Jacobian matrix, which represents the kinematic relationship of the 3-DOF system. **A**

is equal to $\mathbf{BB}^{\mathrm{T}}$, which represents the equivalent relationship between X, Y and θ.

To ensure that the PZTs and the moving platform are not separated during normal operation, the PZTs are installed in slots and connected to the base by the bolt preload. Therefore, the driving force of PZT can be obtained:

$$f_{pzt} = \frac{k_{pzt} \cdot k_c}{k_{pzt} + k_c} d \tag{2}$$

where d is the displacement output of the free PZT is given by:

$$d = d_e V_{pzt} \tag{3}$$

where d_e is a piezoelectric constant, V_{pzt} is the applied voltage. Thus:

$$\begin{bmatrix} \ddot{x} \\ \ddot{y} \\ \ddot{\theta} \end{bmatrix} + 2\begin{bmatrix} \xi_x w_{nx} & 0 & 0 \\ 0 & \xi_y w_{ny} & 0 \\ 0 & 0 & \xi_\theta w_{n\theta} \end{bmatrix}\begin{bmatrix} \dot{x} \\ \dot{y} \\ \dot{\theta} \end{bmatrix} + \begin{bmatrix} w_{nx}^2 & 0 & 0 \\ 0 & w_{ny}^2 & 0 \\ 0 & 0 & w_{n\theta}^2 \end{bmatrix}\begin{bmatrix} x \\ y \\ \theta \end{bmatrix} = \boldsymbol{M}^{-1}\boldsymbol{B}\frac{k_{pzt} \cdot k_c}{k_{pzt} + k_c}\begin{bmatrix} d_{e1} V_{pzt1} \\ d_{e2} V_{pzt2} \\ d_{e3} V_{pzt3} \end{bmatrix} \tag{4}$$

where: $w_{nx}^2 = 3k_{eqx}/2m_{eq}$, $w_{ny}^2 = 3k_{eqx}/2m_{eq}$, $w_{n\theta}^2 = 3r^2 k_{eqx}/I_{zz}$

$2\xi w_{nx} = 3c_{eqx}/2m_{eq}$, $2\xi w_{ny} = 3c_{eqx}/2m_{eq}$, $2\xi w_{n\theta} = 3r^2 c_{eq}/I_{zz}$.

For dynamics modeling, it is usually defines the driving force as the input into the system, which means that the PZT is considered to be a force generator with a spring-damper mass units. However, the PZT has electric characteristics. In [37], Tian proposed that the PZT could be electrically considered as a capacitance with an equivalent circuit. Similar modeling approach has been used in [47-49].

Thus, in this paper, the piezoelectric actuator could be electrically considered as a capacitance with an equivalent circuit as shown in Fig. 6, where $V_{pzt}(t)$ is the actual voltage applied to the piezoelectric actuator, $V_d(t)$ is the input control signal, C, R is the equivalent capacitance and resistance of PZT, respectively. Based on the Kirchhofff's law, the following relationship can be obtained:

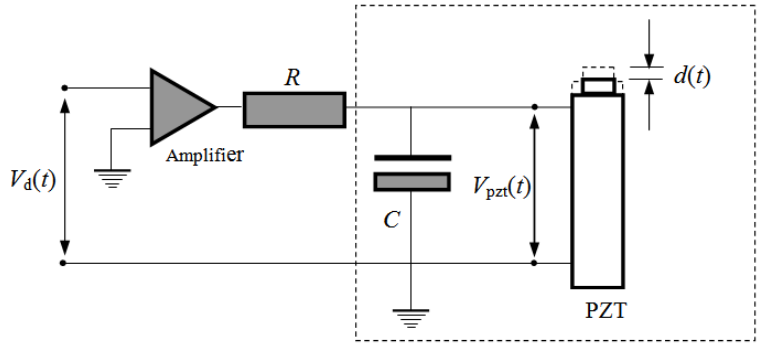

Figure 6 Equivalent driving circuit of the piezoelectric actuator

$$RC\frac{dV_{pzt}(t)}{dt}+V_{pzt}(t)=V_d(t) \tag{5}$$

When the initial input voltage is 0, based on Eq. (5) and it's Laplace transform, the relationship between the input and output can be obtained:

$$V_{\mathrm{pzt}}(s)=\frac{1}{RCs+1}V_{\mathrm{d}}(s) \tag{6}$$

In this case, the signal from input voltage to the output of the displacement in (4) and (6) can be described by a third-order system:

$$\begin{cases} x(s)=\dfrac{d_e\cdot k_{pzt}\cdot k_c/[(k_{pzt}+k_c)\cdot m_{eq}]}{(s^2+2\xi_x\omega_{nx}s+\omega_{nx}^2)(RCs+1)}\left(\dfrac{\sqrt{3}}{2}V_{d2}(s)-\dfrac{\sqrt{3}}{2}V_{d3}(s)\right) \\ y(s)=\dfrac{d_e\cdot k_{pzt}\cdot k_c/[(k_{pzt}+k_c)\cdot m_{eq}]}{(s^2+2\xi_x\omega_{ny}s+\omega_{ny}^2)(RCs+1)}\left(V_{d1}(s)-\dfrac{1}{2}V_{d2}(s)-\dfrac{1}{2}V_{d3}(s)\right) \\ \theta(s)=\dfrac{d_e\cdot r\cdot k_{pzt}\cdot k_c/[(k_{pzt}+k_c)\cdot I_{zz}]}{(s^2+2\xi_\theta\omega_{n\theta}s+\omega_{n\theta}^2)(RCs+1)}\left(V_{d1}(s)+V_{d2}(s)+V_{d3}(s)\right) \end{cases} \tag{7}$$

Thus, the 3-DOF system can be described including both electrical and mechanical characteristics.

3.2 System identification

From Eq. (7), it's known that the parameters for the dynamic model cannot be obtained by simply using the theoretical calculations, because the exact information of the parameters c_{eq}, k_c, R and C is generally incalculable. Therefore, the 3-DOF system

should be identified based on the input control voltage and the corresponding output displacement.

In this study, a sweep signal is employed as the control input, which covers a frequency range from 1 Hz to 3 kHz. In this case, the X and Y axes output displacements are measured and recorded from 0 to 10 s. Fig. 7 shows the frequency spectra of the stage's responses in the X and Y axes, when only the PZT2 is activated. Based on the frequency spectra, the first natural frequencies in the X and Y axes are estimated to be 851.14 Hz and 812.83 Hz, respectively. Compared with the simulation results, experiment results show that the natural frequencies of the stage are increased, it means that the stage has better dynamic characteristics. This is benefited from the installation of PZTs, which increase the stiffness in the actuation directions. In addition, it can be seen that the motion of the 3-DOF stage is coupled.

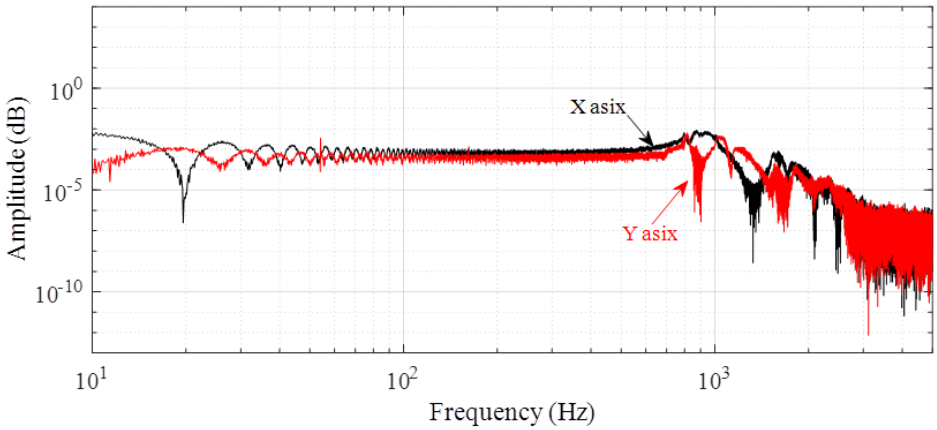

Figure 7 Frequency spectra of the stage's response (only PZT2 is activated)

Based on the system modeled by Eq. (7), the identification is carried out with the Matlab system identification toolbox. During the identification process, the third-order systems are adopted to fit the measured data, and the identified results are given in the following equations:

$$\begin{cases} G_x(s) = \dfrac{-2.16049\times10^6}{s^3+1.0005\times10^6 s^2+5.30864\times10^8 s+3.08642\times10^{13}} \\ G_y(s) = \dfrac{2.65372\times10^6}{s^3+1.00445\times10^6 s^2+5.39141\times10^8 s+3.11251\times10^{13}} \\ G_\theta(s) = \dfrac{9.4302\times10^8}{s^3+5.6032\times10^6 s^2+2.1523\times10^8 s+3.2661\times10^{13}} \end{cases} \tag{8}$$

Fig. 8(a) shows the comparisons the X axis transfer function of the identified model and experimental result. Similar result in the Y axis is obtained. The θ axis transfer function of the identified model and experimental result also is described in Fig. 8(b), and the natural frequencies in the θ axis are estimated to be 945.74 Hz. It can be observed that the identified model can reasonably represent the physical system in the frequency response. However, the deviation exists in the phase plot at high frequencies. One of the reasons is the hysteresis effect, which always causes the phaselag.

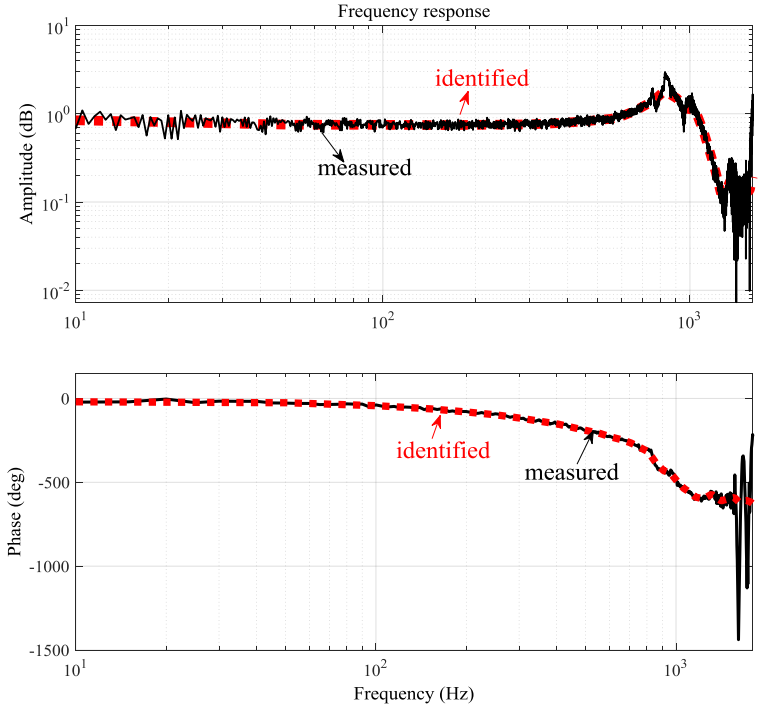

(a)

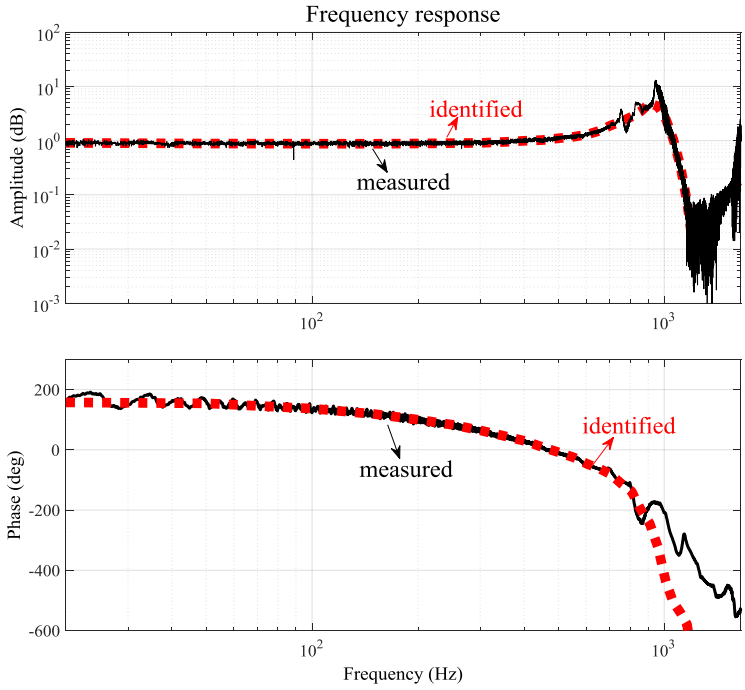

(b)

Figure 8 (a) Frequency response of the transfer function in X axis, and (b) Frequency response of the transfer function in θ axis

4. Experiments and discussions

4.1 Decoupling control

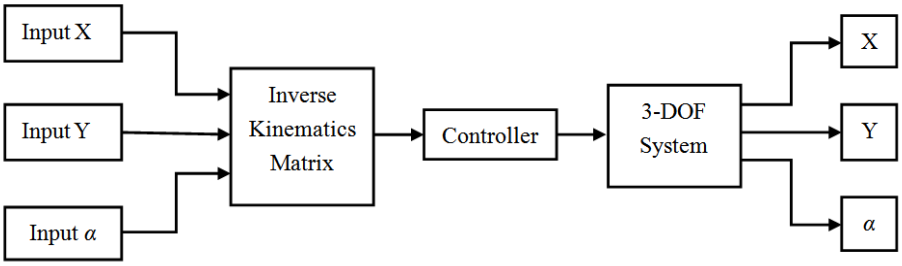

Figure 9 Decoupling control block diagram

As mentioned previously, the motion of the 3-DOF system is coupled. In order to eliminate this coupling, the system is controlled in open-loop via inverse kinematics. The control block diagram is presented in Fig. 9. Therefore, each axis output of the system can be controlled independently when the system is controlled by the simultaneous control of three PZTs.

The motion stroke and coupled motion are tested, and the result is shown in Fig. 10. It can be seen that the maximum translational displacements in the X- and Y-directions are 6.9 μm and 8.6μm, respectively, and rotational motion range is 289 μrad. The decoupling characteristic is confirmed, the maximum coupled displacements in the X- and Y- directions are 0.2346 μm and 0.2752 μm, respectively, and the cross-axis coupling ratio is below 3.5% (3.4% in the X axis, 3.2% in the Y axis), it is mainly due to the assembly errors, manufacture errors and the external disturbances. In this case, the 3-DOF system, which is controlled in open-loop via inverse kinematics can be treated as three Single-Input-Single-Output (SISO) systems.

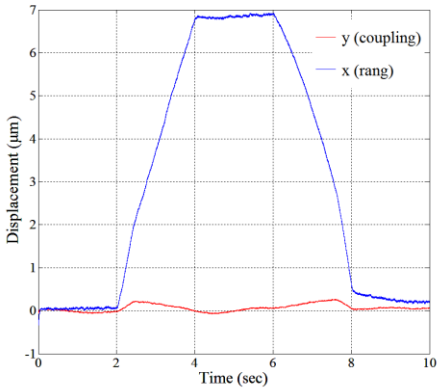

(a)

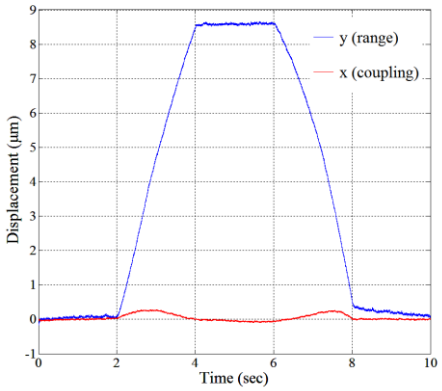

(b)

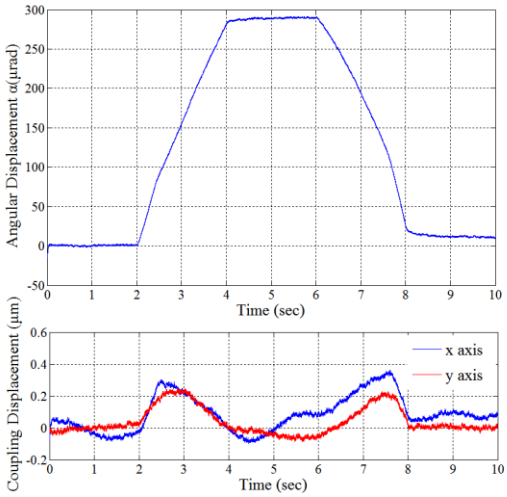

(c)

Figure 10 Experiment test of the motion stroke

4.2 Trajectory tracking

During operations, the control voltage is applied on the PZT, which is defined as the input into the system. Due to the hysteresis and creep effects of the PZT, the relationship between the input control voltage and the output displacement of the PZT is nonlinear. In the literature, many hysteresis models have been developed to describe the hysteresis nonlinearities such as Preisach model [38, 39], Maxwell model [40], Duhem model [41], Bouc-Wen model [42-44], and Prandtl-Ishlinskii model [45]. In this paper, the Bouc-Wen hysteresis model is selected as an illustration. Certainly, other hysteresis models can also be selected. Without loss of generality, it has already been verified that the Bouc-Wen model is suitable to describe the hysteresis loop of PZT [46]. On the other hand, the model is considered in this work since it has fewer parameters. The equation of a B-W model is shown as follows:

$$\dot{h} = ad_e\dot{V}_{pzt} - b\left|\dot{V}_{pzt}\right|h - c\dot{V}_{pzt}|h| \tag{9}$$

where *a*, *b* and *c* are the parameters of this model, *h* is the hysteresis variable. And the parameters identification is implemented by nonlinear least square toolbox running in Matlab environment.

For the proposed 3-DOF stage, the hysteresis can be considered as B-W hysteresis model. It describes the relationship between the input voltage and output displacement. On the contrary, the input voltage used to produce a desired output displacement is solved by its inverse hysteresis model, which will be applied to the piezoelectric actuator. The block diagram of the control with hysteresis compensation is shown in Fig. 11.

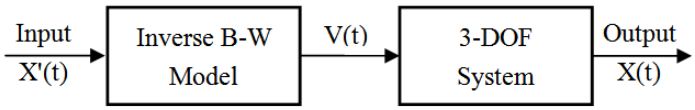

Figure 11 Block diagram of the 3-DOF system with hysteresis compensation

The inverse B-W model can be cascaded to the physical system as a feedforward hysteresis compensator. In order to improve the stability of the tracking performance, a feedback controller is necessary. Therefore, a proportional-integral controller is employed to establish a feedforward-feedback hybrid controller. The schematic diagram of the hybrid controller is proposed in Fig. 12.

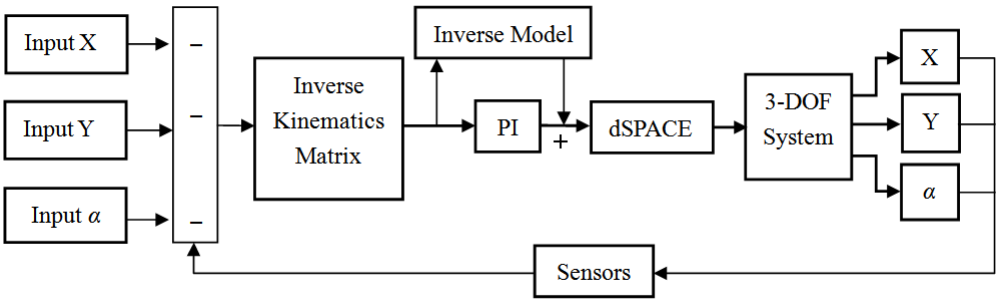

Figure 12 The schematic diagram of the hybrid controller

To test the tracking capability of the 3-DOF system under the hybrid control scheme, sinusoidal trajectory motion tests are conducted to evaluate the tracking performance. Five sinusoidal trajectories with the same amplitude of 6 μm and different frequencies of 0.1, 0.5, 1, 3 and 5 Hz, respectively, are utilized. Due to the symmetry, only the tracking performance in the Y axis is presented. Fig. 13 shows the experimental results on the five sinusoidal trajectories. For trajectories below 1 Hz, as shown in Figs. 13(a), (b) and (c), the maximum tracking errors can be reduced to ±0.1 μm, which can be treated as external noise disturbances. However, for the fast trajectory, as shown in Figs. 13(d) and (e), the maximum tracking errors increases to

±0.2036 and -0.3042 μm, which are as large as 3.393% and 5.07% with respect to the output displacement.

Fig. 14 shows two sinusoidal trajectories tracking on a rotation motion about the Z axis with the same amplitude of 180 μrad and frequencies of 1 and 5 Hz, respectively. The maximum tracking errors ±5.01 μrad and -15.21 μrad are observed in the motion, which are as large as 2.783% and 8.45%, respectively, with respect to the angular displacement.

Based on the above experimental results, we can find that with the increase of the frequency of the input signal trajectory, the tracking capability of the stage is severely decreasing. It means that the tracking errors increase with the increase of the input frequencies. Thus, the method with fixed parameters is only applicable to improve the tracking performance of the stage at low frequencies.

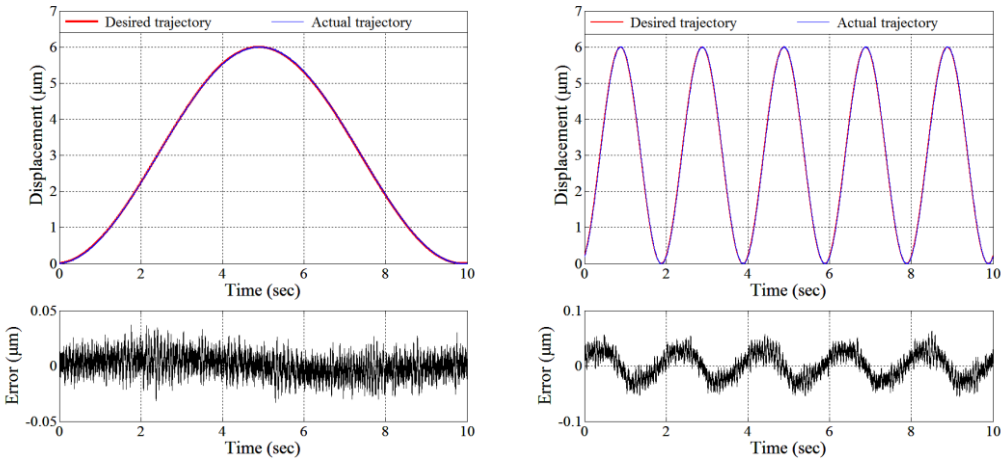

(a) (b)

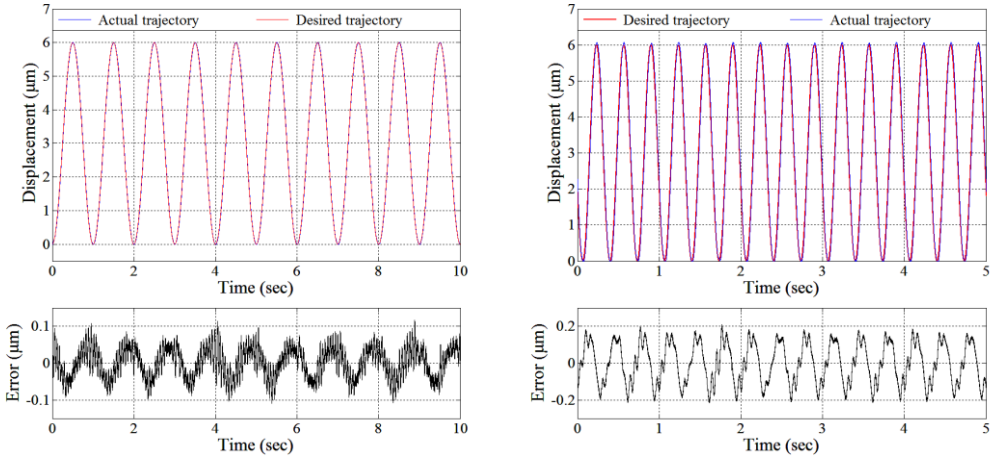

(c) (d)

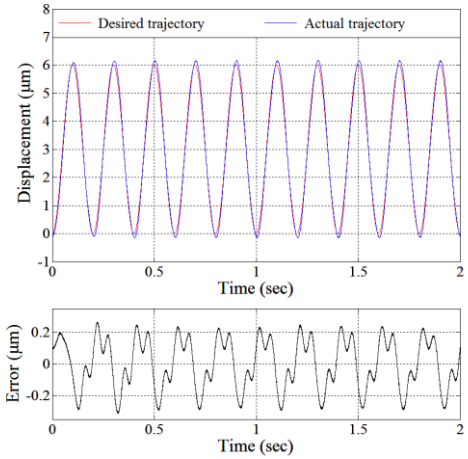

(e)

Figure 13 The result of five different frequencies sinusoidal motion tracking: (a) 0.1 Hz, (b) 0.5 Hz, (c) 1 Hz, (d) 3 Hz and (e) 5 Hz

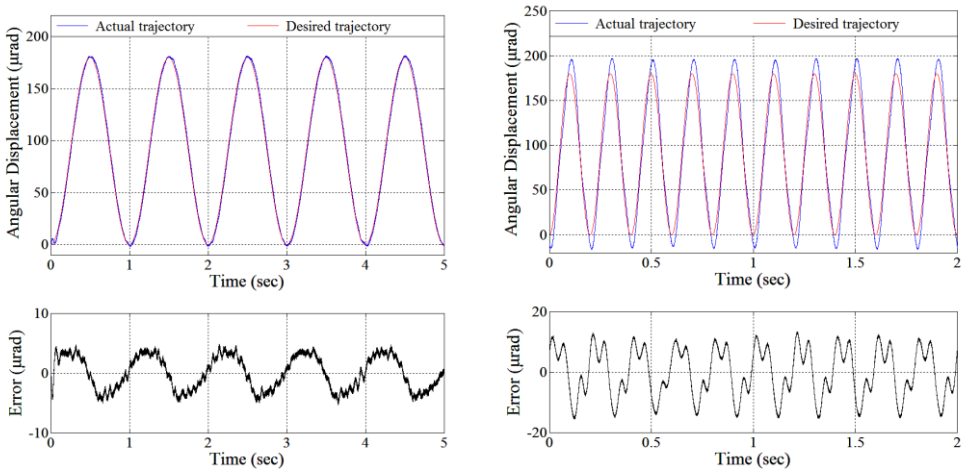

(a) (b)

Figure 14 The result of 1 Hz and 5 Hz sinusoidal motion tracking

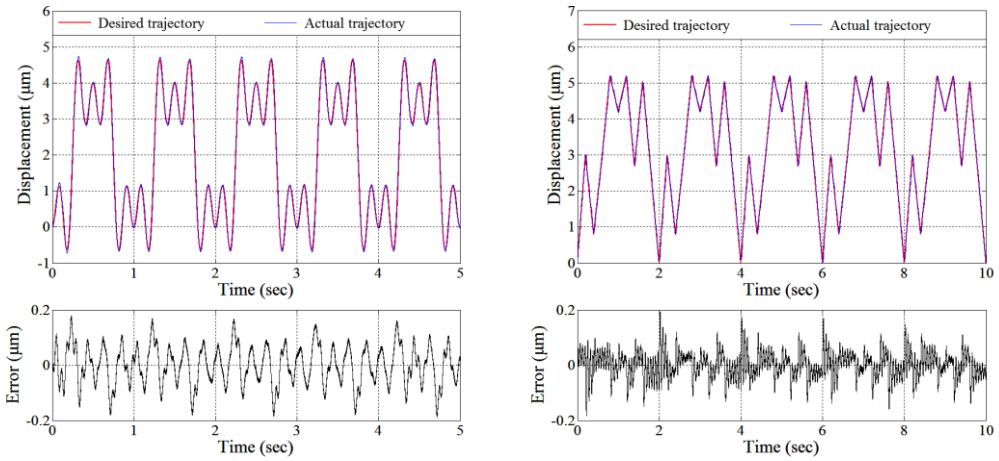

(a) (b)

Figure 15 The result of two superimposed signal tracking: (a) smooth trajectory and (b) non-smooth trajectory

The stage's tracking performance in the Y axis is also verified by tracking two superimposed signal, a smooth trajectory defined by:

$$y(t) = 2 + 2\sin(2\pi t + 1.5\pi) + \sin(6\pi t + 4.5\pi) + \sin(10\pi t + 7.5\pi) \tag{10}$$

Multiple triangular signals are superimposed and selected as other reference trajectories. Period of the non-smooth signal is 2 seconds. The tracking results of the above two trajectories are shown in Fig. 15. Different from the result in smooth trajectories, the large tracking error for this non-smooth signal is found at the corners.

In order to examine the planar trajectory tracking performances of 3-DOF stage, experimental results on the following trajectories are presented: (1) Two circular trajectories of different frequencies centered at point (2.0 μm, 2.0 μm) with a radius of 2.0μm. (2) Two complex trajectories are chosen as the reference trajectories defined by Eqs. (11) and (12), respectively.

$$\begin{cases} x(t) = 3 + 2\sin(\pi t - 0.5\pi) + \sin(8\pi t - 0.5\pi) \\ y(t) = 3 + 2\sin(\pi t) + \sin(8\pi t) \end{cases} \tag{11}$$

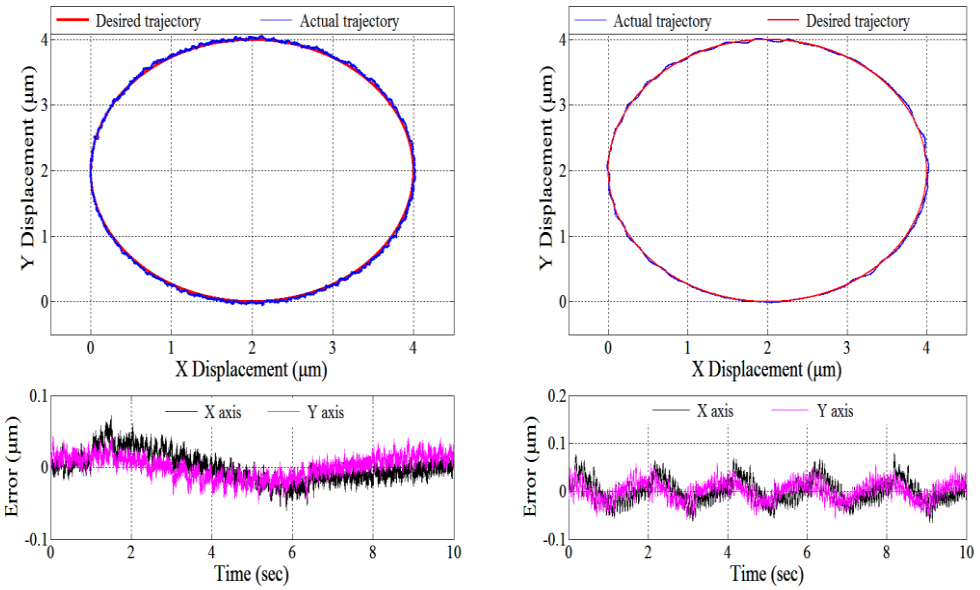

(a) (b)

Figure 16 The result of two different frequencies circular trajectory tracking performance: (a) 0.1 Hz and (b) 0.5 Hz

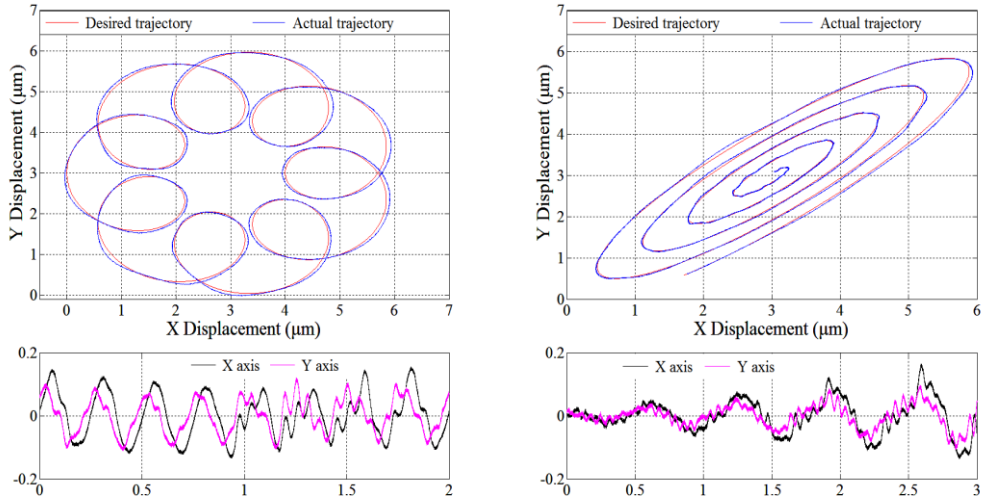

(a) (b)

Figure 17 The result of two complex trajectories tracking performance

$$\begin{cases} x(t) = 3 + (3-t)\sin(3\pi t - 0.15\pi) \\ y(t) = 3 + (3-t)\sin(3\pi t) \end{cases} \tag{12}$$

The experimental results are shown in Figs. 16 and 17. It provides the discrepancies between the desired and actual trajectories. The tracking errors in the X and Y axes are also recorded, respectively.

From the experimental result, for the circular trajectories, it can be obviously observed that the tracking error increases with the increase of the input frequencies. This is similar to uniaxial motion tracking. As shown in Fig. 16(b), the maximum tracking errors (0.0748 μm in X axis and 0.0596 μm in Y axis) with respect to the output displacement are as large as 1.87% in the X axis and 1.49% in the Y axis, respectively. However, for the complex trajectories, as shown in Fig. 17, compared with the circular trajectories, it is found that the tracking performance is unsatisfactory and obviously increased in tracking error. The maximum tracking error (0.1536 μm in the X axis and 0.1069 μmin the Y axis) with respect to the output displacement is as large as 2.56% in the X axis and 1.78% in the Y axis, respectively.

The results of the cross-axis coupling displacement are also obtained in the hybrid controller experiment. The coupled displacements in the X- and Y- directions are 0.175 μm and 0.151 μm, respectively. The cross-axis coupling ratio is 2.91% in the X axis and 2.52% in the Y axis, respectively. This indicates that the proposed closed-loop control methodology can reduce the cross-axis coupling motion and further improve the positioning accuracy.

It is difficult to reduce the tracking error of the 3-DOF system for double axes trajectories. This is because the cross-axis couplings errors. Therefore, the future work is committed to developing suitable controllers that are capable of improving the tracking performance of the stage.

5. Conclusion

A $XY\theta_z$ stage has been developed, and the dynamic modeling, system identification and experimental evaluation for the motion control of the stage have been explored. The obtained conclusions of this paper are summarized as follows:

1) A $XY\theta_z$ stage is designed, and it is driven by three PZTs and guided by three special T-shape hinges. Each T-shape hinge consists of three leaf-spring hinge subsections connected together like a T-joint.

2) Considering both of the electrical and mechanical characteristics, the dynamic model of the 3-DOF stage can be established as a third-order dynamic system to investigate the relationship between the input voltage and the output displacement. The system identification toolbox is utilized to estimate the parameters of the third-order dynamic model.

3) Experimental tests of the prototype stage with the decoupling control are conducted to verify the effectiveness of decoupling control law. The proposed stage has the translation motion strokes of 6.9 and 8.6 μm in the X- and Y-axes, respectively, and rotational range of 289 μrad about the Z-axis. The different motion trajectories are also performed to verify the tracking capability of the stage, which validates good tracking performance of the stage.

Acknowledgement

This research is supported by National Natural Science Foundation of China (Nos. 51275337, 51205279, 51675371, 51420105007), Reserved Academic Program of Peiyang Scholar, and China Scholarship Council.

References

[1] T. Ando. High-speed AFM imaging. Current Opinion in Structural Biology 2014; 28: 63-68.

[2] S. S. Park, M. G. Mostofa, C. I. Park, M. Mehrpouya, S. Kim. Vibration assisted nano mechanical machining using AFM probe. CIRP Annals-Manufacturing Technology 2014; 63 (1): 537-540.

[3] F. Wang, J. Li, S. Liu, X. Zhao, D. Zhang, Y. Tian. An improved adaptive genetic algorithm for image segmentation and vision alignment used in microelectronic bonding, IEEE/ASME Transactions on Mechatronics 2014; 19(3): 916-923.

[4] P. Gao, S. Swei. A six-degree-of-freedom micro-manipulator based on piezoelectric translators, Nanotechnology 1999; 10(4): 447-452.

[5] Y. Tian, B. Shirinzadeh, D. Zhang. Design and dynamics of a 3-DOF flexure-based parallel mechanism for micro/nano manipulation. Microelectronic Engineering 2010; 87(2): 230-241.

[6] J. Paros, L. Weisbord. How to design flexure hinges. Machine Design 1965; (November): 151-156.

[7] Y. Tian, B. Shirinzadeh, D. Zhang. A flexure-based mechanism and control metrology for ultra-precision turning operation. Precision Engineering 2009; 33(2): 160-166.

[8] T. Tomas, H. Walter, R. Hugo, L. John, P. Angeliki and S. Abu. Dual-stage nanopositioning for high-speed scanning probe microscopy. IEEE/ASME TRANSACTIONS ON MECHATRONICS 2014; 19(3): 1035-1045.

[9] F. Makoto, H. Masato, M. Sintaro. Generating sub-nanometer displacement using reduction mechanism consisting of torsional leaf spring hinges. MEASUREMENT SCIENCE REVIEW 2014; 14(1): 48-51.

[10] Q. Xu. A novel compliant micropositioning stage with dual ranges and resolutions. Sensors and Actuators A: Physical 2014; 205(1): 6-14.

[11] Q. Xu. Design and development of a compact flexure-based XY precision positioning system with centimeter range. IEEE TRANSACTIONS ON INDUSTRIAL ELECTRONICS 2014; 61(2): 893-903.

[12] S. Smith, V. Badami, J. Dale, Y. Xu. Elliptical flexure hinges. Review of Scientific Instruments 2000; 68(3): 1474-1483.

[13] Y. Tian, B. Shirinzadeh, D. Zhang. Closed-form compliance equations of filleted V-shaped flexure hinges for compliant mechanism design. Precision Engineering 2010; 34(3): 408-418.

[14] L.L. Howell. Compliant Mechanisms, Wiley, New York, 2001.

[15] B. Trease, Y. Moon, S. Kota.Design of large-displacement compliant joints. ASME Journal of Mechanical Design 2005; 127(4): 788-798.

[16] B.D. Jensen, L.L. Howell. The modeling of cross-axis flexural pivots. Mechanism and Machine Theory 2002; 37(5): 461-476.

[17] M. Goldfarb, J. Speich. The development of a split-tube flexure. The ASME Dynamics and Control Div 2000; 2: 861-866.

[18] S.T. Smith. Flexures: Elements of Elastic Mechanisms, Gordon and Breach Science, New York, 2000.

[19] S. Venanzi, P. Giesen, V. Parenti-Castelli. A novel technique for position analysis of planar compliant mechanisms. Mechanism and Machine Theory 2005; 40(11): 1224-1239.

[20] W.O. Schotborgh, F.G. Kokkeler, H. Tragter. Dimensionless design graphs for flexure elements and a comparison between three flexure elements. Precision Engineering 2005; 29(1): 41-47.

[21] X. Pei, J. Yu, G. Zong, S. Bi, H. Su. The modeling of cartwheel flexural hinges. Mechanism and Machine Theory 2009; 44(10): 1900-1909.

[22] D. Kang, D. Gweon. Analysis and design of a cartwheel-type flexure hinge. Precision Engineering 2013; 37(1): 33-43.

[23] Y. Tian, B. Shirinzadeh, D. Zhang. A flexure-based five-bar mechanism for micro/nano manipulation. Sensors and Actuators A: Physical 2009; 153(1): 96-104.

[24] Y. Tian, B. Shirinzadeh, D. Zhang, X. Liu, D. Chetwynd. Design and forward kinematics of the compliant micro-manipulator with lever mechanisms. Precision Engineering 2009; 33(4): 466-475.

[25] Y. Tian, C. Liu, X. Liu, F. Wang, X. Li, Y. Qin, D. Zhang, B. Shirinzadeh, Design, modeling and characterization of a 2-DOF precision positioning platform, Transactions of the Institute of Measurement and Control (2014), doi: 10.1177/0142331214540692.

[26] Y. Qin, B. Shirinzadeh, Y. Tian, D. Zhang and U. Bhagat. Design and Computational

Optimization of a Decoupled 2-DOF Monolithic Mechanism. IEEE/ASME Transactions on Mechatronics 2014; 19(3): 872-881.

[27] Y. QIN, Y. TIAN, and D. ZHANG. Design and Dynamic Modeling of a 2-DOF Decoupled Flexure-Based Mechanism. CHINESE JOURNAL OF MECHANICAL ENGINEERING 2012; 25(4): 688-696.

[28] F. Wang, Z. Ma, W. Gao, X. Zhao, Y. Tian, D. Zhang, C. Liang. Dynamic modelling and control of a novel XY positioning stage for semiconductor packaging, Transactions of the Institute of Measurement and Control 2015; 37 (2): 177-189.

[29] F. Wang, X. Zhao, D. Zhang, et al. Robust and precision control for a directly-driven XY table. Proceedings of the Institution of Mechanical Engineers, Part C: Journal of Mechanical Engineering Science 2011; 225(5): 1107-1120.

[30] F. Wang, X. Zhao, D. Zhang, et al. Design and control of a high-acceleration precision positioning system using a novel flexible decoupling mechanism. Proceedings of the Institution of Mechanical Engineers, Part C: Journal of Mechanical Engineering Science 2010; 224(2): 431-442.

[31] S. Polit, J. Dong. Development of a high-bandwidth XY nanopositioning stage for high-rate micro/nano manufacturing, IEEE/ASME Transactions on Mechatronics 2011; 16(4); 724-733.

[32] Y. Qin, B. Shirinzadeh, D. Zhang, Y. Tian. Design and kinematics modeling of a novel 3-DOF monolithic manipulator featuring improved Scott-Russell mechanisms. Journal of Mechanical Design 2013; 135(10): 101004-1-101004-9.

[33] Z. Guo, Y. Tian, C. Liu, F. Wang, X. Liu, B. Shirinzadeh, D. Zhang. Design and control methodology of a 3-DOF flexure-based mechanism for micro/nano positioning, Robotics and Computer Integrated Manufacturing 2015; 32: 93-105.

[34] H. Kim and D. Gweon. Development of a compact and long range XYθz nano-positioning stage. REVIEW OF SCIENTIFIC INSTRUMENTS 2012; 83(8): 085102-1-085102-8.

[35] U. Bhagat, B. Shirinzadeh, L. Clark, P. Chea, Y. Qin, Y. Tian, D. Zhang. Design and analysis of a novel flexure-based 3-DOF mechanism. Mechanism and Machine Theory 2014; 74: 173-187.

[36] H. Kim, D. Ahn, and D. Gweon. Development of a novel 3-degrees of freedom flexure based positioning system. REVIEW OF SCIENTIFIC INSTRUMENTS 2012; 83(5): 055114-1-055114-11.

[37] Y. Tian, D. Zhang, B. Shirinzadeh, Dynamic modelling of a flexure-based mechanism for ultra-precision grinding operation. Precision Engineering 2011; 35(4): 554-565.

[38] Y. Ting, H.-C.Jar and C.-C. Li, Measurement and calibration for Stewart micromanipulation system, Precision Engineering 2007; 31(3): 226-233

[39] Boukari A-F, Carmona J-C, Moraru G, Malburet F, Chaaba A, Douimi M. Piezoactuators modeling for smart applications. Mechatronics 2011; 21(1): 339-349.

[40] Juhasz L, Maas J, Borovac B. Parameter identification and hysteresis compensation of embedded piezoelectric stack actuators. Mechatronics 2011; 21(1): 329-338.

[41] C. Lin, P. Lin. Tracking control of a biaxial piezo-actuated positioning stage using generalized Duhem model. Computers and Mathematics with Applications 2012; 64(5): 766-787.

[42] M. Rakotondrabe. Bouc-Wen modeling and inverse multiplicative structure to compensate hysteresis nonlinearity in piezoelectric actuators. IEEE Transactions on Automation and Engineering 2011; 8(2): 428-431.

[43] Y.-T. Liu, K.-M. Chang and W.-Z. Li. Model reference adaptive control for a piezo-positioning system. Precision Engineering 2010; 34(1): 62-69.

[44] J. Park and W. Moon. Hysteresis compensation of piezoelectric actuators: The modified Rayleigh model. Ultrasonics 2010; 50(3): 335-339.

[45] X. Y. Zhang and Y. Lin. Adaptive tracking control for a class of pure-feedback non-linear systems including actuator hysteresis and dynamic uncertainties. IET Control Theory and Applications 2011; 5(16): 1868-1880.

[46] T. S. Low and W. Guo. Modeling of a three-layer piezoelectric bimorph beam with hysteresis. J. MEMS 1995; 4(4): 230-237.

[47] M. Goldfarb and N. Celanovic. Modeling piezoelectric stack actuators for control of micromanipulation. IEEE Control Syst. Mag. 1997; 17(3): 69-79.

[48] H. J. M. T. A. Adriaens, W. L. D. Koning, and R. Banning. Modeling piezoelectric actuators. IEEE/ASME Trans. Mechatronics 2000; 5(4): 331-341.

[49] Y. S. Gao, D. W. Zhang, and C. W. Yu. Dynamic modeling of a novel workpiece table for active surface grinding control. Int. J. Mach. Tools Manuf. 2001; 41(4): 609-624.